Drying Technology
An International Journal

ISSN: 0737-3937 (Print) 1532-2300 (Online) Journal homepage: www.tandfonline.com/journals/ldrt20

Spray drying of highly viscous feeds: Modeling the internal flow of an ACLR atomizer for non-Newtonian liquid feeds with high dry-matter contents

Miguel Ángel Ballesteros Martínez & Volker Gaukel

To cite this article: Miguel Ángel Ballesteros Martínez & Volker Gaukel (2025) Spray drying of highly viscous feeds: Modeling the internal flow of an ACLR atomizer for non-Newtonian liquid feeds with high dry-matter contents, Drying Technology, 43:11-12, 1824-1832, DOI: 10.1080/07373937.2025.2534037

To link to this article: https://doi.org/10.1080/07373937.2025.2534037

Published online: 17 Jul 2025.

DRYING TECHNOLOGY
2025, VOL. 43, NOS. 11–12, 1824–1832
https://doi.org/10.1080/07373937.2025.2534037

Taylor & Francis
Taylor & Francis Group

Spray drying of highly viscous feeds: Modeling the internal flow of an ACLR atomizer for non-Newtonian liquid feeds with high dry-matter contents

Miguel Ángel Ballesteros Martínez and Volker Gaukel

Institute of Process Engineering in Life Sciences: Food Process Engineering, Karlsruhe Institute of Technology, Karlsruhe, Germany

ABSTRACT

Spray drying is a widely used method for producing food powders in large quantities, but it also has a high energy demand. To address this, researchers aim to increase the dry-matter content of liquid feeds, which poses the challenge of having to atomize high-viscosity liquids into fine droplets. The Air-Core-Liquid-Ring (ACLR) nozzle offers a solution by inducing an internal annular flow, though it can present internal instabilities. This study numerically investigates how high feed viscosities, of up to 1.3 Pa · s, influence the internal flow conditions. We confirmed that, even at this viscosity range, the internal instabilities can be strongly reduced while maintaining air-to-liquid ratios below 1 and pressures below 1 MPa. This is much lower than pressures of pressure-swirl nozzles and ALRs of external-mixing nozzles, which are both more commonly used in the industry. A CFD model was successfully adapted to predict the internal flow behavior and it can be used to evaluate process conditions outside experimental capabilities.

ARTICLE HISTORY
Received 10 March 2025
Revised 3 July 2025
Accepted 9 July 2025

KEYWORDS
Spray drying; high viscosity; ACLR; CFD; non-Newtonian modeling

1. Introduction

Drying processes are known to be the most energy-consuming type of unit operation in the food industry.[1] An EU-Project showed that 12–25% of the total industrial energy consumption in many developed countries can be attributed to industrial drying.[2] In the field of food powders, most products available on the market are manufactured using a spray dryer.[3] A straightforward way to reduce energy consumption is to increase the dry-matter content that can be fed to the atomizer. According to a model calculation on industrial spray drying done by Fox et al.,[3] an increase in the feed dry-matter content by just 1% leads to a decrease in the thermal energy consumption of the spray dryer of 3.8% and an increase in powder production capacity of 4.5%. Unfortunately, increasing the feed dry-matter content also increases the feed viscosity, which can cause complications in the atomization step,[4] leading to blockages or large droplet sizes. In turn, the large droplet sizes can lead to depositions in the drying tower, incomplete drying, or inhomogeneous powder properties.[5] Therefore, it is important to select a nozzle design that is capable of handling high viscosities.

One promising nozzle design that can fulfill this role is the Air-Core-Liquid-Ring (ACLR) nozzle,[6] which is a type of internal-mixing pneumatic nozzle. The device is composed of two concentric tubes. The outer casing is where the liquid feed flows, while a capillary at the center carries the compressed air and injects it in a mixing chamber. This favors the formation of an annular flow, with a liquid lamella (or ring) around the air core. As this two-phase flow exits the nozzle, the air phase expands, and the liquid film forms a cone that breaks up into droplets.[7]

The two-phase flow inside the atomizer allows it to handle liquids with higher viscosities than pressure-swirl nozzles,[6] which means that it can handle more concentrated feeds with higher dry-matter contents. Based on this, Wittner et al.[4] estimated that the ACLR nozzle can reduce total energy consumption in a spray-drying process (counting the pre-concentration of the feed, the atomization step and the drying process) by up to 29%, compared to a process using a standard pressure-swirl nozzle. On top of that, because the gas and liquid flows are combined inside the nozzle,[8] lower gas flowrates are possible compared to

CONTACT Miguel Ángel Ballesteros Martínez miguel.ballesteros@kit.edu Institute of Process Engineering in Life Sciences: Food Process Engineering, Karlsruhe Institute of Technology, Karlsruhe, Germany

external-mixing atomizers.[9] A lower atomizing gas flowrate leads to reduced operating costs and should lead to a higher heat transfer efficiency inside the drying tower.[10]

Nonetheless, the ACLR nozzle can suffer from internal flow instabilities, which become more significant at high viscosities and are also known to affect the resulting droplet sizes. Stähle, Gaukel, and Schuchmann[6] and Wittner et al.[11] identified that increasing viscosities increased both the Sauter mean diameter (SMD) and its temporal unsteadiness. Wittner et al.[11] concluded that this is a direct consequence of the viscosity increasing the thickness and instability of the liquid lamella inside the nozzle, although they only evaluated maltodextrin solutions with viscosities up to 390 mPa·s with dry-matter contents up to 47% wt.

A helpful way to understand these internal flow instabilities is using computational fluid dynamics (CFD). The usefulness of CFD for the analysis of spray drying has long been identified.[12] However, existing studies tend to focus on the drying step and its kinetics, using simplified correlations to model the atomization step.[13,14] In our previous work, we developed a CFD model to study the unstable flow conditions inside the ACLR nozzle, but it was developed and validated only for Newtonian liquids and viscosities only up to 140 mPa · s.[15] Experimental and rheological measurements, as presented in Ballesteros Martinez et al.,[16] has shown that solutions with dry-matter contents above 47% wt. present a strong shear-thinning behavior. This means that the existing model had to be adapted with a non-Newtonian formulation, and that the system had to be validated again with experimental data. The implementation of the updated CFD model and its subsequent validation are the purpose of this present work.

2. Materials and methods

2.1. Rheology of the maltodextrin solutions

To validate the CFD model, experiments were carried out with aqueous solutions of maltodextrin C*DryTM MD 01958 (dextrose equivalent = 8.8, Cargill Deutschland GmbH, Düsseldorf, Germany). The viscosity of the maltodextrin solution was measured with a rotational rheometer (Physica MCR 301, Geometry DG26.7, Anton Paar, Graz, Austria) at shear rates between 1 to 10^3 s $^{-1}$. The measurements were complemented with measurements with a capillary rheometer Rheograph 6000 (GÖTTFERT Werkstoff-Prüfmaschinen GmbH, Buchen, Germany), at shear rates from 10^3 to 10^6 s $^{-1}$. The complete viscosity profiles for the maltodextrin solutions

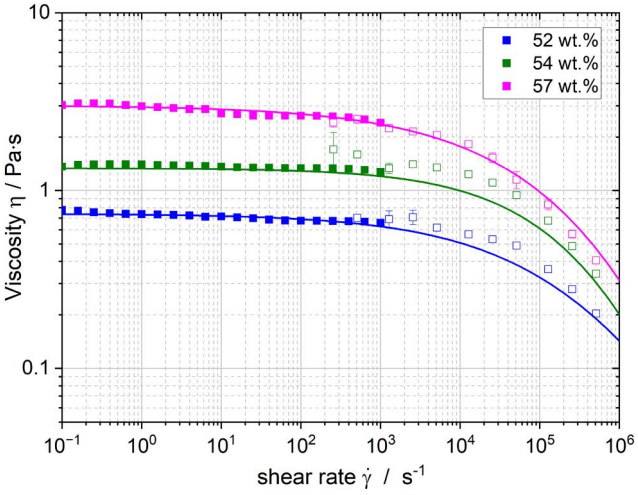

Figure 1. Viscosity of the maltodextrin solutions at different concentrations. Full symbols represent data from a rotational rheometer, while empty symbols represent data from a capillary rheometer. Adapted from Ballesteros Martinez et al.[16]

are shown in Figure 1. A strong shear-thinning behavior can be seen for all solutions. In general, the rotational and capillary measurements overlap well. All rheology measurements, as well as all experiments and simulations, were conducted at 25 °C.

2.2. Spray test rig

All experiments were carried out in a spray test rig, which has been described in detail in our previous study.[16] In short, it is composed of a closed cabin with a vertical atomizer on top. The liquid flow is supplied by an eccentric screw pump and measured by a gear flow meter. Air is supplied by a compressor. The air pressure is adjusted with a pressure regulator, and its resulting volume flow is measured by a gas flow meter. The outer casing of the ACLR is built of clear acrylic. This allowed the direct optical visualization of the flow conditions inside the atomizer using a high-speed video camera and a high-performance light-emitting diode system. The camera recorded the internal flow at a frame rate of 20 kHz. Each measurement was composed of 10,000 images, which amounts of 0.5 s measurement time. The exposure time of each image was 5 µs, and the resolution was around 10 µm/pixel. The images were processed with a Matlab code to measure the thickness of the liquid film, i.e. lamella, inside the nozzle. The algorithm of the code is described in detail in Wittner et al.[11] To statistically characterize the lamella thickness variation, the 5%, 50% and 95% percentiles, which are denoted as $h_{5,0}$, $h_{50,0}$, and $h_{95,0}$, respectively, were calculated for each combination of pressure and viscosity.

3. Numerical modeling

The CFD model, including the physics models and the mesh, was implemented in STAR-CCM+ v.2206 (Siemens AG, Munich, Germany) as described in our previous work.[15] The multiphase flow that develops in the nozzle was modeled as an immiscible mixture of two phases: The liquid phase was set as incompressible with the non-Newtonian rheology model, while the gas phase was assumed as ideal and Newtonian.

3.1. Governing equations

The multiphase flow was simulated using the Volume-Of-Fluid (VOF) method. This model assumes that all fluid phases share the same pressure and velocity fields. This means that the two-phase system is modeled as a single-phase fluid, whose physical properties are calculated from the volume averages of the properties of the actual phases.[17] This means that only one momentum equation, like the one shown in Equation 1 is solved to predict the velocity and pressure fields of the mixture.

$$\frac{\mathrm{d}}{\mathrm{d}t}\int_V \rho\mathbf{u}\mathrm{d}V + \int_A \rho\mathbf{u}\otimes\mathbf{u}\cdot\mathrm{d}\mathbf{A} = -\int_A p\boldsymbol{I}\cdot\mathrm{d}\mathbf{A} + \int_A \boldsymbol{\tau}\cdot\mathrm{d}\mathbf{A} + \int_V \mathbf{f_b}\mathrm{d}V \qquad (1)$$

On the left side of the equation are the terms for transient and convective transport. $\mathbf{u}$ is the velocity, while ρ represents the volume-averaged density. On the right side of the equation are the pressure gradient term, the viscous stress term, and external body force term. Correspondingly, p is the local pressure, $\boldsymbol{\tau}$ is the stress tensor, and $\mathbf{f_b}$ is the external body force vector. $\boldsymbol{I}$ is the identity matrix. As for the integrals, V represents the volume; conversely, $\mathbf{A}$ is the normal vector of the surface area. Finally, t is the time.Using the VOF formulation, the internal flow was modeled as transient because of the unstable free surface between the phases.

Additionally, to account for turbulence, the Large Eddy Simulation model (LES) was used. With LES, the flow variables are decomposed spatially into a filtered value and a subgrid component.[18,pp.53–71] By introducing these decomposed variables into the transport equations, the filtered variables can be resolved directly. In contrast, the subgrid stresses are modeled indirectly, estimating them from the filtered values and a turbulent subgrid viscosity. There are different options to determine the turbulent viscosity. From the recommendations of the user guide,[19] the Wall-Adapting Local-Eddy Viscosity (WALE) Subgrid Scale model was selected.[20] The WALE model does have the limitation that it includes a user-defined coefficient that is not universal. However, the default value of 0.1 seems to work well for most common applications, so it was not altered.[19] An all-y^+ wall treatment was also included to improve turbulence modeling in the near-wall region.

The choice of the LES model was based on previous analysis of the multiphase flow inside the ACLR nozzle. This analysis encompassed comparing both Reynolds-Average Navier-Stokes (RANS) methods and LES.[15,21] In short, it was found that the fluctuating annular flow inside the ACLR nozzle was better captured with LES, while using RANS led to a stronger underprediction of the oscillations and waviness that the flow presents. The RANS approach is mostly suited to predict the average thickness of the liquid lamella inside the nozzle, while LES gave a more accurate prediction of the range of fluctuation that could be expected.

3.2. Mesh generation

The mesh configuration and density was based on the mesh independence analysis done on our previous study, which was performed for a quarter of a nozzle.[21] In short, the regions of interest, i.e. the mixing chamber and the outlet channel, were meshed with a fine polyhedral grid. Conversely, the inlet regions upstream, where there is exclusively either gas or liquid, were fitted with a coarser hexahedral grid. To define the optimal mesh density, four meshes were generated in that study, each with a different reference cell size but with the same number of prism layers. The cell size ranged from 33–42 μm. The thickness of the first prism layer was calculated following good practice recommendations by White.[22,p.467] The convergence criteria were the average lamella thickness inside the outlet channel and the ALR. The axial velocity profile was also compared between the meshes, to evaluate the spatial resolution of the grids. The finest mesh evaluated, noted as M4, fulfilled the requirements indicated for the LES modeling, so it was the mesh utilized for this study. The adequacy of the mesh was determined using the Kolmogorov and Taylor length scales, which are a good criteria for the minimum and maximum local cell sizes, respectively, that an appropriate mesh should have. More details about this analysis can be found in Ballesteros Martínez, Becerra, and Gaukel.[15] The chosen mesh

has a reference cell size of 33 μm, a cell count of 1.3 million cells, and it can be seen in Figure 2.

3.3. Boundary and simulating conditions

The boundary and initial conditions were set up following the same procedure from our previous work.[15] The boundary conditions set for the simulation are shown in Figure 2. Just as in the experimental setup, the gas pressure and the liquid flowrate were the inlet boundary conditions set in the simulations. The exit of the simulated volume was set as an atmospheric pressure outlet. Because only half the nozzle was simulated, a symmetry plane was implemented.

An adaptive timestep implemented in the model ensures the stability of the solver.[21] The timestep was configured to ensure a maximum Courant–Friedrichs–Lewy (CFL) number of 1. The timestep usually stabilized around 50 ns. For every timestep, the convergence criterion was that the absolute residuals reached values below 10^{-3}, which was usually achieved within 20 iterations. All simulations were run for at least 8 ms. We accounted for 4 ms of initialization time and used the other 4–5 ms of simulated time for the time-dependent and time-averaged analysis. These times were based on our previous calculations in Ballesteros Martínez and Gaukel,[21] which account for the phase velocities and the frequency of the internal flow oscillation noticed in experiments. For reference, a simulation required around 10 days of computing while running with 80 cores at the high-performance computer system BwUnicluster 2.0 (Baden-Württemberg, Germany).

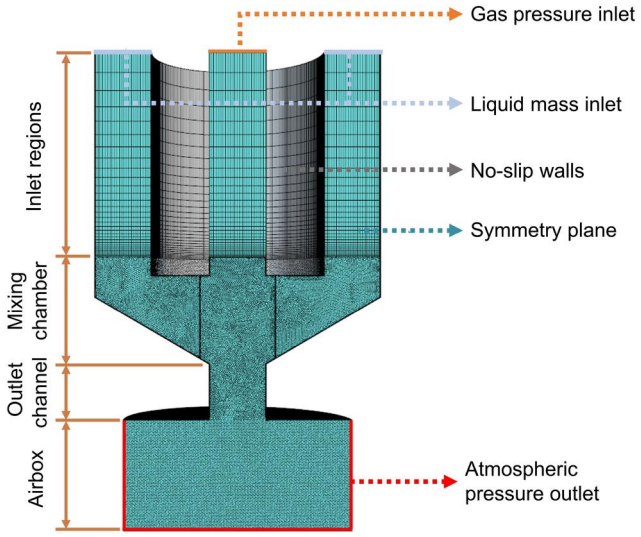

Figure 2. Simulated mesh of the ACLR atomizer. The boundary conditions are also indicated. Taken from Ballesteros Martínez and Gaukel.[23]

3.4. Non-Newtonian modeling

To better characterize the shear-thinning behavior, we fitted the rheological measurements with the Carreau-Yasuda model.[24,25] The equation of the model is the following:

$$\eta(\dot{\gamma}) = \eta_{\infty}(\eta_0 - \eta_{\infty})\left(1 + (\lambda \cdot \dot{\gamma})^a\right)^{(n-1)/a} \quad (2)$$

where η is the viscosity, η_0 is the zero viscosity, η_{∞}, the viscosity at infinite shear rate, and $\dot{\gamma}$ is the shear rate. The correlation parameters are the relaxation time λ, the power index n, and the parameter a, which control the shear-thinning behavior. Table 1 shows the model parameters that result from the regression fit to the experimental data. The model seems to fit well with the experimental measurements, with most R^2 being above 0.9. The increase in the η_0 with higher dry-matter content of maltodextrin highlights the increasing viscosity of the mixtures. Similarly, the decreases in λ and n signal the increasing shear-thinning behavior of the solutions, as the maltodextrin fraction becomes higher.

3.5. Operating conditions

Table 2 shows the operating conditions that were used in the atomization experiments and in the simulations. It must be mentioned that the viscosities of the maltodextrin solutions were at the limit and/or outside the ideal operation range of the pump. This is the reason why the flowrates are different for various solutions. At this range of viscosities, any increase in the solution viscosity affects the pump performance and the flowrates that the pump can achieve. In addition to this, higher viscosities also affect the stability with which the pump can deliver a specific flowrate. This can be noticed with the deviation values given for the flowrates, which also strongly increase with the solution viscosity. For the simulations, the underlined pressures indicate those for which there was experimental data available for validation. Not all three maltodextrin solutions were simulated, as it was not feasible to obtain reliable time-stable operating conditions when atomizing the 57% wt. solution that could be use for validation. Nonetheless, the three

Table 1. Fitting parameters for the Carreau-Yasuda model for maltodextrin concentrations.

Dry-matter content [% wt.]	η_0 [Pa · s]	η_{∞} [Pa · s]	λ [s]	n [–]	a [–]	R^2 [–]
52	0.74	0	1.03	0.10	0.38	0.95
54	1.33	0	0.49	−0.60	0.46	0.92
57	3.01	0	0.08	−1.22	0.35	0.99

Table 2. Operating conditions utilized in experiments (EXP) and simulations (SIM). The zero viscosity is mentioned again for reference. Underlined pressures indicate that there was experimental data available.

			Pressure [MPa]	
Dry-matter content [% wt.]	η_0 [Pa · s]	Flowrate [L · h $^{-1}$]	SIM	EXP
52	0.74	25 ± 2	0.4, 0.7 and 1.0	0.2, 0.4, 0.6, and 0.7
54	1.33	15 ± 2	0.7, 1.0 and 1.5	
57	3.01	2–12[a]	—	

[a]The flowrate tended to vary around 10±2 L · h $^{-1}$ for a couple seconds but would suddenly decrease to 2 L · h $^{-1}$, then return to 10 L · h $^{-1}$.

solutions were analyzed experimentally in a separate study,[16] to evaluate the applicability of the ACLR nozzle for highly viscous feeds.

Furthermore, the objective of developing such a CFD model is not only to recreate the atomization conditions that can be observed in the experiments, but also to be able to evaluate conditions outside of the limits of the experimental setup. This is especially important with respect to the air pressure, which has been identified as the limiting operating factor when it comes to atomizing high viscosities.[23] That means that the necessary pressure to stably atomize a liquid strongly increases with the liquid viscosity. The experimental setup can only reach pressures up to 0.7 MPa, so additional simulations at 1.0 and 1.5 MPa were performed. In total, six simulations were carried out: three for validation and three extrapolating to conditions outside the experimental capabilities.

4. Results and discussion

As mentioned before, the objective of this study was both to validate the adapted CFD model using experimental data and to use the CFD model to evaluate operating conditions that were not reachable with the experimental setup. For that purpose, we compared the ALRs measured in the experiments with those obtained in the simulations. After all, the ALR is a vital process parameter for pneumatic nozzles.[7] These values are shown in Table 3. As expected, the simulated ALRs increase with pressure, just as it happens in the experiments. It can also be noticed that the ALR increases at a constant pressure of 0.7 MPa, when the maltodextrin concentration increases. This is related to the lower flowrate that could be achieved with the pump in the experiments, and, consequently, the lower flowrate that was set in the simulations.

The specific values are relatively similar between simulations and experiments. There is a more noticeable difference at 54% wt. compared to the rest. Nonetheless, the standard deviation of the experiment and simulation results are larger, so the difference in the averages might not be as significant. It is also

Table 3. Average experimental (EXP) and simulated (SIM) Air-to-Liquid-Ratios (ALR) with standard deviations.

		ALR [–]	
Dry-matter content [% wt.]	Pressure [MPa]	EXP	SIM
52	0.4	0.11 ± 0.02	0.10 ± 0.04
	0.7	0.23 ± 0.04	0.18 ± 0.04
	1.0	—	0.38 ± 0.06
54	0.7	0.38 ± 0.06	0.27 ± 0.05
	1.0	—	0.38 ± 0.06
	1.5	—	0.84 ± 0.10

interesting to note that the variation of the ALR increases with pressure. The larger pressure difference along the nozzle might cause the air compressibility to play a larger role, which may cause local variations of the air velocity and cause some fluctuations in the ALR.

Looking at the extrapolated conditions, the two simulations at 1.0 MPa seem to reach the same ALR, even if they have a different liquid flowrate and solution concentration. It is not yet clear if this is a matter of coincidence, or if the effect of viscosity on the ALR becomes less important as the air pressure increases. Further increasing the pressure to 1.5 MPa leads to a strong rise in the ALR, although it still remains below 1. This means that it would still operating below the usual ALR values of external-mixing nozzles.

Apart from the ALR, we used the lamella thickness as a validation parameter, since it is also the most important flow variable that we would like to obtain from any extrapolated operating conditions. The experimental values are shown in Figure 3. The figure shows the lamella variation range (shown as the shaded area between $h_{5,0}$ and $h_{95,0}$) for the three different solutions at different ALRs. The $h_{50,0}$ is also shown in the middle of the shaded area. These experimental results are also shown in Ballesteros Martínez et al.,[16] but to reiterate: The most evident observation is that all solutions, regardless of their very different viscosities, show similar thickness values for the same ALRs, and they all seem to decrease at the same rate as the ALR increases. This is a positive sign of the process intensification capabilities of the ACLR that nozzle.

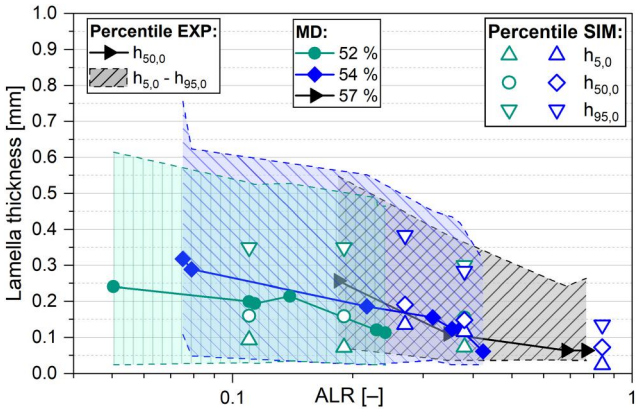

Figure 3. Lamella thicknesses of different maltodextrin (MD) concentrations (indicated with the different colors and markers) at increasing ALRs. For experiments (EXP), the median ($h_{50,0}$) is indicated by full symbols connected by lines. The 5% and 95% percentiles ($h_{5,0}$ and $h_{95,0}$) are indicated as the shaded regions. The percentiles for the simulation (SIM) results are shown as empty symbols.

For comparison, the percentiles of the lamella thicknesses from the simulations are also shown in Figure 3. In general, the simulation results fall within the same range as the experimental measurements. The simulated $h_{50,0}$ values overlap well with the experimental data for all cases. Furthermore, at least for 54% wt., they follow the expected trend: there is a clear decrease of the lamella thickness and its range of variation ($h_{5,0}$–$h_{95,0}$) with increasing ALRs. This is especially noticeable at 1.5 MPa, where there seems to be very little remaining variation of the lamella thickness, which is much more remarkable considering that the ALR, as shown in Table 3, remains below 1. In comparison, studies with air-blast nozzles, regardless of whether they worked with viscosities of 2 mPa · s[26] or 1000 mPa · s,[27] report ALRs between 1–15.

However, it must be mentioned that the decreasing trend is not as clear for the 52% wt. solution, at least at the pressures of 0.4 and 0.7 MPa (ALR: 0.11 and 0.19). The decrease at 1.0 MPa (ALR: 0.38) is slightly more noticeable. One contributing reason to this deviation might come from the fact that the wall-treatment models from STAR-CCM+ were all developed for Newtonian fluids.[19] This models are based on the assumption that the turbulent boundary layers can be decomposed into four different regions, similar to what was described by Kovasznay[28]: a viscous sub-layer, a log layer, an outer turbulent layer, and an outer edge interface. However, Loureiro and Silva Freire[29] found that this assumption does not necessarily work for non-Newtonian fluids, especially Carreau fluids. In spite of this, we considered it more valuable to include turbulence modeling, even if the wall-treatment models were not theoretically applicable, rather than assuming a laminar flow. That is especially true considering that the Reynolds number for the gas flow is around 10^5.[21]

With that in mind, we instead explored other methods of analysis, to see what further information we could gain about the flow instabilities from the simulations, particularly for the maltodextrin solution that presented the deviation: 52% wt. To that effect, the moment-to-moment profiles of the lamella thicknesses were plotted as shown in Figure 4. For 0.4 and 0.7 MPa, sections from the experimental measurements are also included. One must keep in mind that the time scale and resolution of the simulations and the experiments are different. Simulations are run for a short time span of 4 ms, but with a small timestep of ~50 ns. In contrast, experiments are run for a far larger timestep of 500 ms but with a much lower time resolution of 50 µs. The lower time resolution of the experiments is easily noticed in Figure 4: Compared to the simulations, the individual experimental points are relatively far apart from each other. The different time resolution affects how the flow behavior shows on both profiles, and it means a direct comparison should should be considered with caution. Nonetheless, the visual analysis can provide valuable information about the flow instabilities. For the simulations, there seems to be a very marked pulsating behavior. As the pressure increases, the peaks draw closer to each other and begin overlapping. By 1.0 MPa, it is much more difficult to distinguish the peaks from each other compared to 0.4 MPa.

Given that these peaks should be responsible for the calculated $h_{95,0}$, we characterized their average height and width at the different pressures. This is shown in Table 4. Similarly to the time-dependent profiles seen in Figure 4, the peak period decreases with pressure, as their frequency increases. More importantly, the simulated average peak height does decrease with pressure, which is the flow behavior that we expected. It agrees with the experimental percentiles shown in Figure 3: Higher pressures, i.e., higher ALRs, lead to lower flow variation. It is not clear why this does not reflect on the simulated $h_{95,0}$ from Figure 3, but that might just be a consequence of the short simulation time span.

Performing a similar analysis for the experimental results is difficult, because the data points are sparser. Therefore, we were not certain that we could reliably measure some average peak height or width. Qualitatively speaking, the experimental profile at 0.4 MPa seems to also show the pulsating behavior

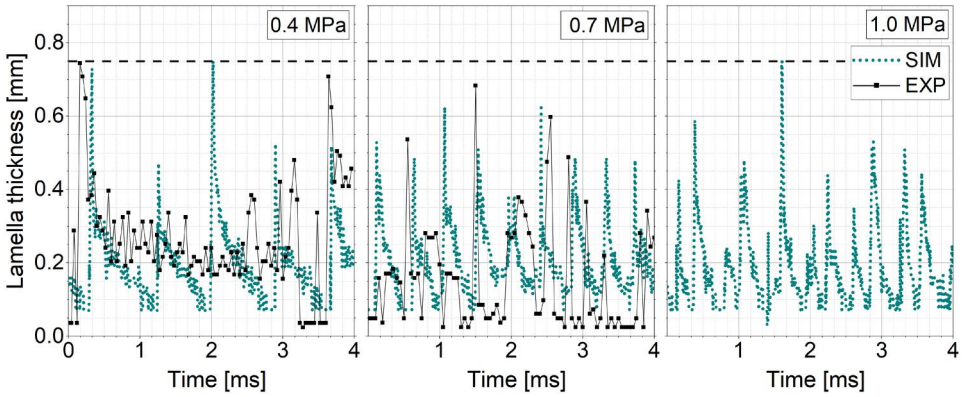

Figure 4. Time-dependent lamella thickness profiles of a 52% wt. maltodextrin solution different pressures. The profiles shown correspond to simulations (SIM) and experiments (EXP). The nozzle radius is represented as a dashed black line.

Table 4. Peak information from the simulated lamella thickness profiles.

Pressure [MPa]	Avg. peak height [mm]	Peak separation [ms]
0.4	0.60	0.80
0.7	0.51	0.44
1.0	0.43	0.31

seen in the simulations. There are two clear peaks (where the lamella thickness reaches the nozzle radius) separated by around 3.5 ms. Comparatively, the profile at 0.7 MPa seems much more chaotic, although the maximum values observed seem to match the peaks seen for the simulations. Given the limited time resolution in the experiments, the authors place more trust in the simulation predictions, at least with respects to the moment-to-moment behavior in the short time spans, even if the accuracy of turbulence modeling might be compromise by the non-Newtonian behavior of the liquid.

5. Conclusions

A CFD model was successfully adapted in STAR-CCM+ v.2206 to predict the internal flow of non-Newtonian maltodextrin solutions being atomized with an ACLR nozzle. In general, the predicted ALRs from the simulations agree with what was observed in experiments. Additionally, the liquid lamella thickness inside the nozzle follows the same trend in the simulations as what is observed in experiment: A smaller internal lamella variation is observed as the ALR increases. Nonetheless, it must be noted that there are some deviations between simulation and experiments. For the ALR, the main deviation happens for the higher maltodextrin concentration. In this case, experimental uncertainty may also play a role in the deviation, since the pump had difficulties maintaining a stable flowrate at this range of viscosities. For the lamella thickness, the deviation happened at the lower ALRs of the 52% wt. solution. Looking at the moment-to-moment profiles, it may be that the strongly pulsating behavior of the flow is not well captured by the statistical percentiles because of the short simulation time span. In general, the large difference in the time span and time resolution of experimental measurements and simulation results make statistical comparison difficult, although comparing and characterizing the moment-to-moment profiles did bring more valuable information. An additional source of error might be that the available turbulence wall-treatment models were not formulated for non-Newtonian liquids. In spite of this, we concluded that a less-accurate turbulence modeling was considered preferable to omitting turbulence modeling completely. Moreover, the possibility of using simulations to evaluate operating conditions outside of experimental capabilities were also evidenced. The lamella variation can be severely reduced by increasing the operating pressure to 1.5 MPa, which is still far below the 5–25 MPa that is common in pressure-swirl nozzles.

Acknowledgements

The researchers would like to thank the support by the state of Baden-Württemberg through access to the bwHPC.

Disclosure statement

No potential conflict of interest was reported by the author(s).

Funding

This work was partly funded by the Deutsche Akademische Austauschdienst (DAAD), through one of their research grants for doctoral programs in Germany. The authors also acknowledge the financial support of the International Fine Particle Research Institute (IFPRI).

References

[1] Đaković, D.; Kljajić, M.; Milivojević, N.; Doder, Đ.; Anđelković, A. S. Review of Energy-Related Machine Learning Applications in Drying Processes. *Energies* **2023**, *17*, 224. DOI: 10.3390/en17010224.

[2] Claussen, I. C.; Sannan, S.; Bantle, M.; Lauermann, M.; Wilk, V. "DryFiciency Waste Heat Recovery in Industrial Drying Processes." *Specification of Performance Indicators and Validation Requirements*; Technical Report D1.2; EU Project No.: 723576; European Union, **2021**. https://dryficiency.eu/wp-content/uploads/2021/08/D1_2_Performance-indicators-and-validation-requirements_Update-Scanship.pdf.

[3] Fox, M.; Akkerman, C.; Straatsma, H.; Jong, P. Energy Reduction by High Dry Matter Concentration and Drying. *New food* **2010**, *6*, 60–62. https://www.newfoodmagazine.com/article/474/energy-reduction-by-high-dry-matter-concentration-and-drying/.

[4] Wittner, M. O.; Karbstein, H. P.; Gaukel, V. Energy Efficient Spray Drying by Increased Feed Dry Matter Content: Investigations on the Applicability of Air-Core-Liquid-Ring Atomization on Pilot Scale. *Drying Technol.* **2020**, *38*, 1323–1331. DOI: 10.1080/07373937.2019.1635616.

[5] Gogate, P. R. The Use of Ultrasonic Atomization for Encapsulation and Other Processes in Food and Pharmaceutical Manufacturing. In *Power Ultrasonics*; Woodhead Publishing: Cambridge, **2015**; pp 911–935.

[6] Stähle, P.; Gaukel, V.; Schuchmann, H. P. Comparison of an Effervescent Nozzle and a Proposed Air-Core-Liquid-Ring (ACLR) Nozzle for Atomization of Viscous Food Liquids at Low Air Consumption. *J. Food Process Eng.* **2017**, *40*, 12268. DOI: 10.1111/jfpe.12268.

[7] Wittner, M. O.; Karbstein, H. P.; Gaukel, V. Spray Performance and Steadiness of an Effervescent Atomizer and an Air-Core-Liquid-Ring Atomizer for Application in Spray Drying Processes of Highly Concentrated Feeds. *Chem. Eng. Process. Process Intensif.* **2018**, *128*, 96–102. DOI: 10.1016/j.cep.2018.04.017.

[8] Wozniak, G. T. Z. In *Zerstäubungstechnik*; Wozniak, G., Ed.; Springer: Berlin, Heidelberg, **2003**; pp 57–87.

[9] Hammad, F. A.; Sun, K.; Jedelsky, J.; Wang, T. The Effect of Geometrical, Operational, Mixing Methods, and Rheological Parameters on Discharge Coefficients of Internal-Mixing Twin-Fluid Atomizers. *Processes* **2020**, *8*, 563. DOI: 10.3390/pr8050563.

[10] Anandharamakrishnan, C.; Ishwarya, S. P. *Spray Drying Technique for Food Ingredient Encapsulation*; Wiley-Blackwell, IFT Press: Chichester; Hoboken, NJ, **2015**.

[11] Wittner, M. O.; Ballesteros, M. A.; Link, F. J.; Karbstein, H. P.; Gaukel, V. Air-Core–Liquid-Ring (ACLR) Atomization Part II: Influence of Process Parameters on the Stability of Internal Liquid Film Thickness and Resulting Spray Droplet Sizes. *Processes* **2019**, *7*, 616. DOI: 10.3390/pr7090616.

[12] Jamaleddine, T. J.; Ray, M. B. Application of Computational Fluid Dynamics for Simulation of Drying Processes: A Review. *Drying Technol.* **2010**, *28*, 120–154. DOI: 10.1080/07373930903517458.

[13] Bürger, J. V.; Jaskulski, M.; Kharaghani, A. Modeling of Maltodextrin Drying Kinetics for Use in Simulations of Spray Drying. *Drying Technol.* **2025**, *43*, 214–227. DOI: 10.1080/07373937.2024.2421451.

[14] Kemp, I. C.; Hartwig, T.; Herdman, R.; Hamilton, P.; Bisten, A.; Bermingham, S. Spray Drying with a Two-Fluid Nozzle to Produce Fine Particles: Atomization, Scale-up, and Modeling. *Drying Technol.* **2016**, *34*, 1243–1252. DOI: 10.1080/07373937.2015.1103748.

[15] Ballesteros Martínez, M. A.; Becerra, D.; Gaukel, V. Modelling the Flow Conditions and Primary Atomization of an Air-Core-Liquid-Ring (ACLR) Atomizer Using a Coupled Eulerian–Lagrangian Approach. *Flow. Turbulence Combust.* **2024**, *113*, 437–458. DOI: 10.1007/s10494-024-00555-1.

[16] Ballesteros Martínez, M. A.; Roy, P.; Solano Alarcón, J. N.; Gaukel, V. Atomizing High-Viscosity non-Newtonian Fluids with the ACLR Nozzle: Correlation between Internal Flow and External Spray Instabilities. *J. Non-Newtonian Fluid Mech.* **2025**, *338*, 105405. DOI: 10.1016/j.jnnfm.2025.105405.

[17] Sun, S.; Zhang, T. Review of Classical Reservoir Simulation. In *Reservoir Simulation: Machine Learning and Modeling*; Gulf Professional Publishing: Cambridge, MA, **2020**; pp 23–86.

[18] Baker, C.; Johnson, T.; Flynn, D.; Hemida, H.; Quinn, A.; Soper, D.; Sterling, M. *Train Aerodynamics*; Butterworth-Heinemann: Oxford, **2019**.

[19] Siemens Industries Digital Software. Simcenter STAR-CCM+ User Guide, version 2206, **2022**. https://plm.sw.siemens.com/en-US/simcenter/fluids-thermal-simulation/star-ccm/.

[20] Nicoud, F.; Ducros, F. Subgrid-Scale Stress Modelling Based on the Square of the Velocity Gradient Tensor. *Flow, Turbulence and Combustion* **1999**, *62*, 183–200. DOI: 10.1023/A:1009995426001.

[21] Ballesteros Martínez, M. A.; Gaukel, V. Time-Averaged Analysis and Numerical Modelling of the Behavior of the Multiphase Flow and Liquid Lamella Thickness Inside an Internal-Mixing ACLR Nozzle. *Flow. Turbulence Combust.* **2023**, *110*, 601–628. DOI: 10.1007/s10494-023-00406-5.

[22] White, F. M. *Fluid Mechanics*, 8th ed.; McGraw-Hill: New York, NY, **2016**.

[23] Ballesteros Martínez, M. A.; Gaukel, V. Understanding the Operating Limitations of an Internal-Mixing Air-Core-Liquid-Ring (ACLR) Nozzle for Process Intensification in Spray Drying. *Drying Technol.* **2024**, *42*, 2087–2094. DOI: 10.1080/07373937.2024.2328300.

[24] Carreau, P. J. Rheological Equations from Molecular Network Theories. *Transactions of the Society of Rheology* **1972**, *16*, 99–127. DOI: 10.1122/1.549276.

[25] Yasuda, K.; Armstrong, R. C.; Cohen, R. E. Shear Flow Properties of Concentrated Solutions of Linear and Star Branched Polystyrenes. *Rheol. Acta* **1981**, *20*, 163–178. DOI: 10.1007/BF01513059.

[26] Tareq, M. M.; Dafsari, R. A.; Jung, S.; Lee, J. Effect of the Physical Properties of Liquid and ALR on the

Spray Characteristics of a Pre-Filming Airblast Nozzle. *Int. J. Multiphase Flow* **2020**, *126*, 103240. DOI: 10.1016/j.ijmultiphaseflow.2020.103240.

[27] Mansour, A.; Chigier, N. Air-Blast Atomization of non-Newtonian Liquids. *J. Non-Newtonian Fluid Mech.* **1995**, *58*, 161–194. DOI: 10.1016/0377-0257(95)01356-Z.

[28] Kovasznay, L. S. G. Structure of the Turbulent Boundary Layer. *The Physics of Fluids* **1967**, *10*, S25–S30. DOI: 10.1063/1.1762462.

[29] Loureiro, J.; Silva Freire, A. Asymptotic Analysis of Turbulent Boundary-Layer Flow of Purely Viscous Non-Newtonian Fluids. *J. Non-Newtonian Fluid Mech.* **2013**, *199*, 20–28. DOI: 10.1016/j.jnnfm.2013.05.003.